Supplemental Materials: Constraints on Axion-like Particles from a Hard X-ray Observation of Betelgeuse

BETELGEUSE STELLAR MODELS

The total ALP number per time and energy can be obtained integrating Eq. (2) over the volume of the star, $d\dot{N}_a/dE = \int (d\dot{n}_a/dE) dV$. We find that, with an excellent approximation, the ALP source spectrum has the following form [S1]

$$\frac{d\dot{N}_a}{dE} = \frac{10^{42} C g_{11}^2}{\mathrm{keV\ s}} \left(\frac{E}{E_0}\right)^{\beta} e^{-(\beta+1)E/E_0} \ , \tag{S1}$$

where $g_{11} = g_{a\gamma}/10^{-11}\,\mathrm{GeV}^{-1}$, while C is the normalization, E_0 coincides the average energy, and β is the spectrum index. The values of C, E_0 and β depend on various structural parameters characterizing the core of the star, such as temperature, density and chemical composition. To this aim, we will make use of stellar models computed using the FuNS code (see [S2] for a detailed description of this code and the adopted input physics). Alpha Orionis (Betelgeuse) is a red supergiant whose luminosity, effective temperature and metallicity are, respectively, $\log L/L_\odot = 5.10 \pm 0.22$ ([S3]), $T_{\rm eff} = 3641 \pm 53\,\mathrm{K}$ ([S4]), and $[\mathrm{Fe/H}] = +0.1 \pm 0.2$ ([S5]). These data constrain the initial mass between 18 and 22 $M_\odot$, in good agreement with previous determinations ([S6, S7]). We note that the uncertainty of Betelgeuse mass contributes much smaller effect for ALP-photon production than the time to core collapse or B_T, and is thus ignored here. In our analysis we adopted a model of 20 $M_\odot$ with solar composition.

Extant models of stars with mass ~ 20 M$_\odot$ may evolve to the red supergiant stage at the onset or at the end of the core-He burning, depending on the assumed efficiency of the semiconvective mixing (see the discussion in section 2.2 in [S2]). In the FuNS model, scarce semiconvective mixing is usually assumed, so that the star becomes a red supergiant since the beginning of the core-He burning. This phase lasts for $\sim 8 \times 10^5$ yrs, during which the central temperature and density remain more or less the same. After the core He is exhausted, the stellar luminosity increases and attains a maximum value during the C-burning phase. After that, the luminosity remains constant, until the final core collapse. However, during this phase, which lasts a few 10^4 yrs, the temperature and the density within the core undergo constant and substantial increases. In turn, a significant increase of the ALP-production rate is expected (the ALP production rate is a steep function of the temperature).

Since the precise evolutionary status cannot be determined from the observed stellar properties, we have considered a set of stellar models taken at different times before the core-collapse. All of these stellar models match the observed L and $T_{\rm eff}$. In this way we may trace the expected evolution of the ALP flux during the red supergiant phase of Betelgeuse. The luminosity, the central temperature and the time to the core collapse of these models are reported in Tab. S1. Model 0 assumes Betelgeuse is still in the core-He burning phase; models 1–4 are before C burning; models 5–9 are during the C burning; model 11 is during the Ne burning; and model 12 is at the beginning of the O burning. Fig. S1 illustrates the temperature profiles of some of the 13 models for the most internal 6 $M_\odot$.

Model	Phase	$t_{\rm cc}$ [yr]	$\log_{10}(L_{\rm eff}/L_\odot)$	$\log_{10}(T_{\rm eff}/\mathrm{K})$	C	E_0 [keV]	β
0	He burning	155000	4.90	3.572	1.36	50	1.95
1	before C burning	23000	5.06	3.552	4.0	80	2.0
2	before C burning	13000	5.06	3.552	5.2	99	2.0
3	before C burning	10000	5.09	3.549	5.7	110	2.0
4	before C burning	6900	5.12	3.546	6.5	120	2.0
5	in C burning	3700	5.14	3.544	7.9	130	2.0
6	in C burning	730	5.16	3.542	12	170	2.0
7	in C burning	480	5.16	3.542	13	180	2.0
8	in C burning	110	5.16	3.542	16	210	2.0
9	in C burning	34	5.16	3.542	21	240	2.0
10	between C/Ne burning	7.2	5.16	3.542	28	280	2.0
11	in Ne burning	3.6	5.16	3.542	26	320	1.8
12	beginning of O burning	1.4	5.16	3.542	27	370	1.8

TABLE S1. Models of ALP production from Betelgeuse. The stage of stellar evolution is parameterized by the time remaining until the core collapse for Betelgeuse, $t_{\rm cc}$. See text for the definition of other parameters.

By folding Eq. (3) from Eq. (2), (4) and (5), the differential photon flux per unit energy arriving at Earth can be

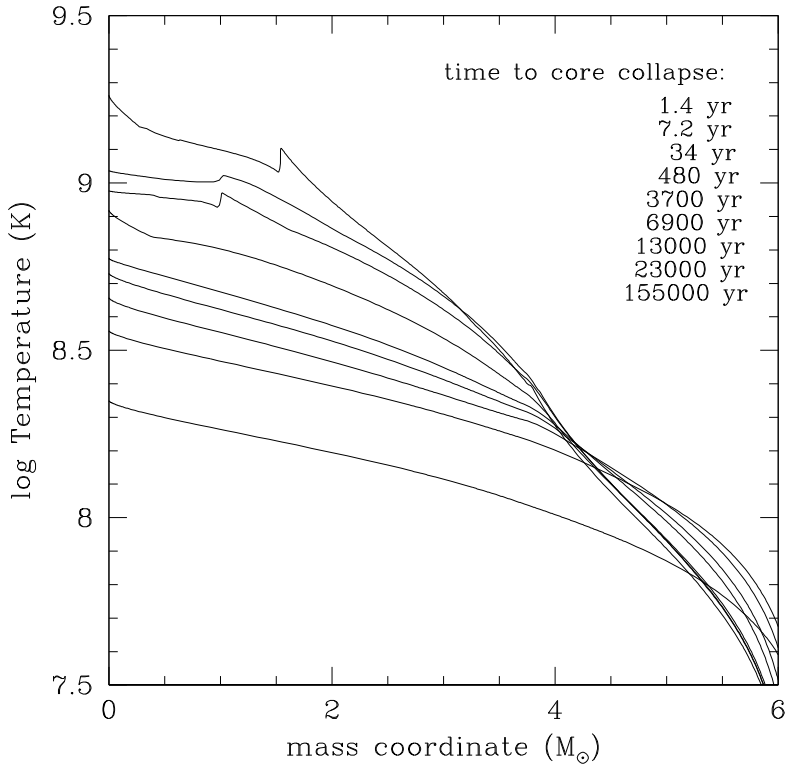

FIG. S1. Temperature profiles of some of the 13 models in Tab. S1. The plot shows the most internal 6 $M_\odot$ of each model. As the star approaches the final core collapse, the temperature becomes steeper within the core, so that the ALPs production progressively becomes more centrally concentrated. The model labelled 155000 yr to the collapse refers to the He-burning phase, while that 480 yr to the C-burning phase and 1.4 yr to the collapse is taken at the beginning of the O burning. The secondary temperature peaks shown by some models are due to the presence of active C or Ne burning shells.

numerically calculated :

$$\frac{dN_\gamma}{dEdSdt} = \frac{g_{11}^4}{\mathrm{keV\,cm^2\,s}} \left(\frac{C}{5.36\times10^5}\right) \left(\frac{E}{E_0}\right)^\beta e^{-(\beta+1)E/E_0} \left(\frac{B_T}{1\ \mu G}\right)^2 \left(\frac{d}{197\ pc}\right) \frac{\sin^2 q}{q^2}\,, \tag{S2}$$

where

$$q \simeq \left[77\left(\frac{m_a}{10^{-10}\,\mathrm{eV}}\right)^2 - 0.14\left(\frac{n_e}{0.013\ \mathrm{cm^{-3}}}\right)\right] \times \left(\frac{d}{197\,\mathrm{pc}}\right)\left(\frac{E}{1\,\mathrm{keV}}\right)^{-1}\,,$$

Using the fitted parameters in Tab. S1, Fig. S2 shows the predicated X-ray spectra before and after *NuSTAR* instrument response for typical ALP masses in this work.

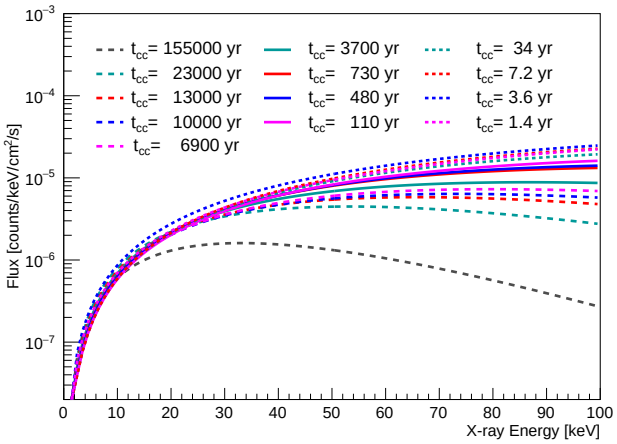

(a)$m_a = 1.0 \times 10^{-11}$ eV (before *NuSTAR*)

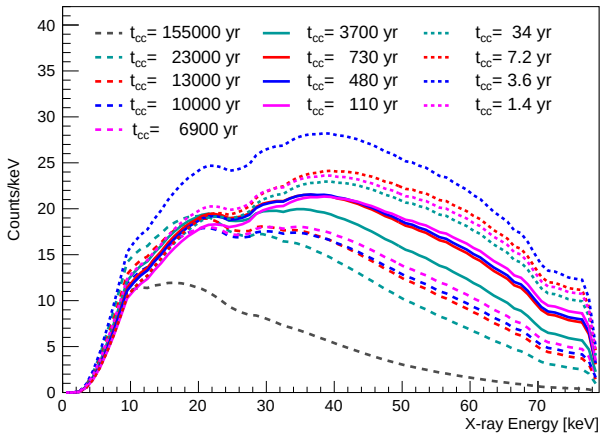

(b)$m_a = 1.0 \times 10^{-11}$ eV (after *NuSTAR*)

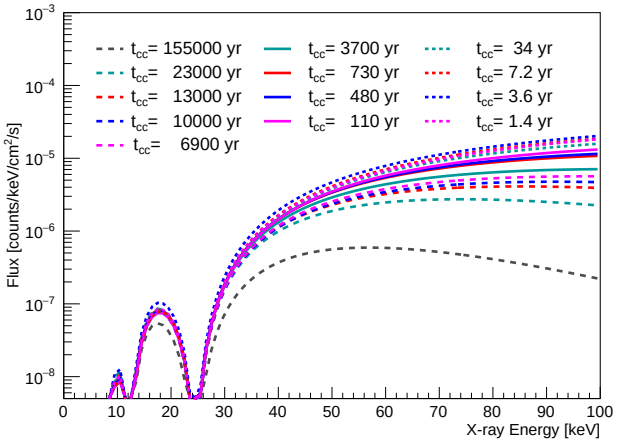

(c)$m_a = 1.0 \times 10^{-10}$ eV (before *NuSTAR*)

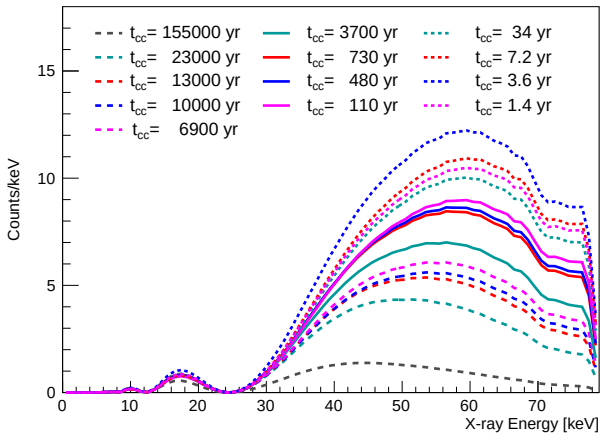

(d)$m_a = 1.0 \times 10^{-10}$ eV (after *NuSTAR*)

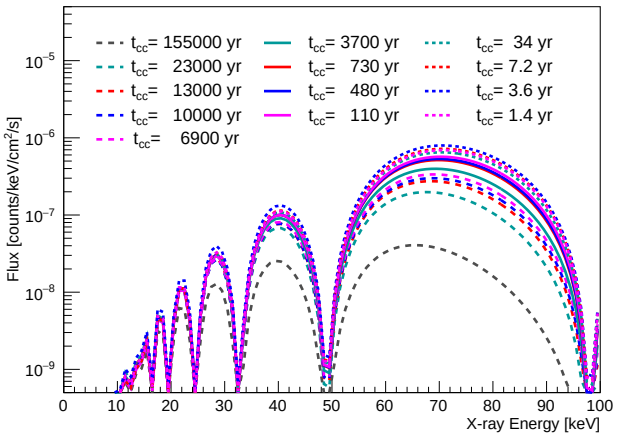

(e)$m_a = 2.0 \times 10^{-10}$ eV (before *NuSTAR*)

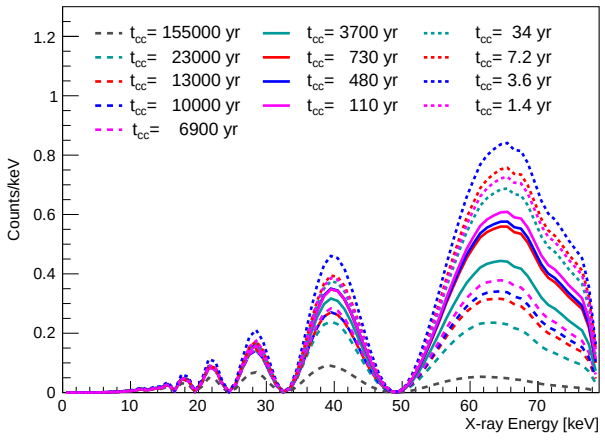

(f)$m_a = 2.0 \times 10^{-10}$ eV (after *NuSTAR*)

FIG. S2. Predicated X-ray spectra *before* and *after* *NuSTAR* instrument response with ALP-photon production models for representative ALP masses with assumption of $B_T = 1.4\ \mu G$ and $g_{a\gamma} = 1.5 \times 10^{-11}\ GeV^{-1}$.

NUSTAR BACKGROUND MODELING

The *NuSTAR* instrument background spectral model contains several components, which may be broadly categorized as having astrophysical or detector origins. Our ALP search does not require a detailed parametrization of the *NuSTAR* instrument background, so we summarize the most important aspects here and refer the reader to Refs. [S8, S9] for a detailed description. Our primary concern is the uniformity of the instrument background between the source spectral extraction region and the background spectral extraction region. The background components that are known to have significant spatial variation across the detector arrays are the unfocused cosmic X-ray background (CXB) and X-rays from fluorescence/activation of the instrument structure. The CXB level is observed to be nearly uniform on the sky for the angular and energy acceptance of a single *NuSTAR* observation [S10, S11], but the shadowing effects of the optics bench and aperture stops produce a radially-varying intensity pattern for the unfocused CXB. The intensity of the detector background is known to vary between the detector chips, though is largely constant within each chip [S8]. Both the unfocused CXB gradient and the detector emission motivate the choice of a background region as close as possible to—and ideally on the same detector chip as—the source region, as shown in Fig. S3.

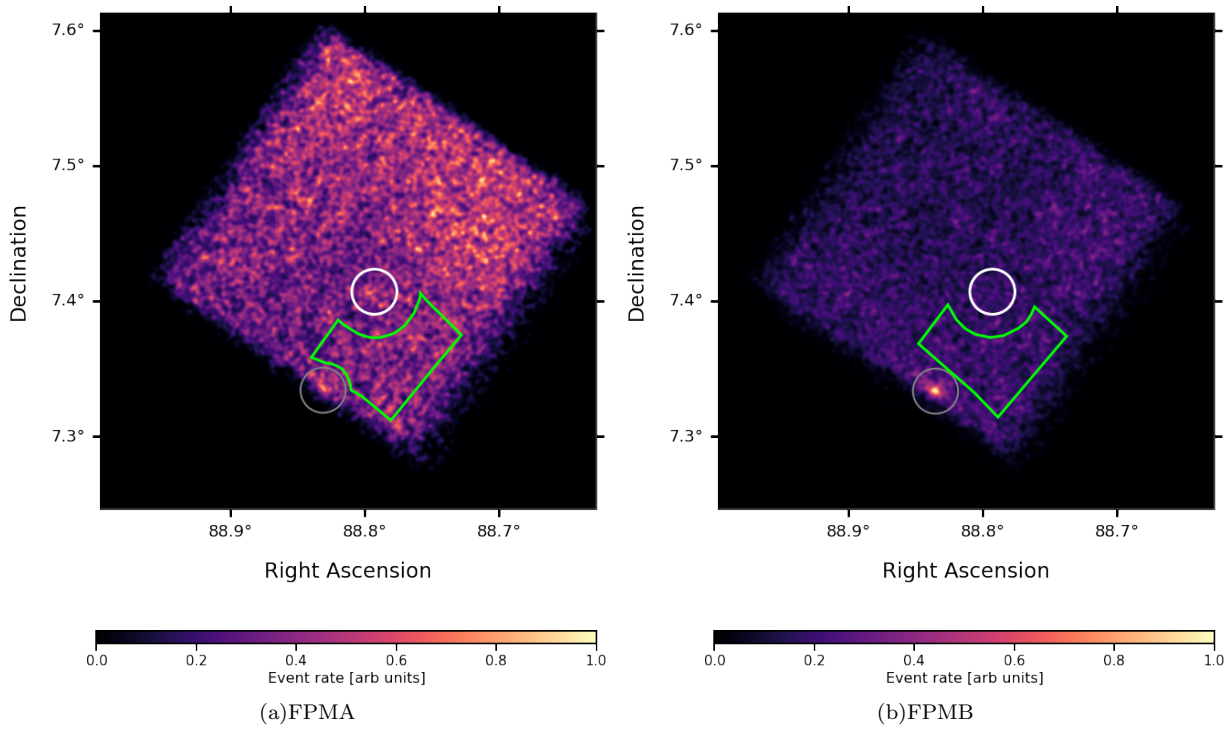

FIG. S3. FPMA (left) and FPMB (right) images of *NuSTAR* observation regions in the energy range 3–79 keV, the event rate in each image is the relative value to the highest one and the image is smoothed with a 2-dimensional Gaussian of width $\sigma = 4.5''$ for presentation. The Betelgeuse source region (white circle, $60''$ radius) and background region (green polygon, at least $120''$ from Betelgeuse) are shown. The far-away point source is indicated with gray circle ($60''$ radius).

We further confirm the spatial uniformity of background by comparing the X-ray spectra with different choices of background region on the same detector chip. In addition to the polygon region shown in Fig. S3, we also choose the other two circle regions ($60''$ radius) which are $120''$ away from the Betelgeuse center. Using the data process described above, we extract the X-ray spectrum in each background region. Fig. S4 compares the spectra from three background regions after the normalization of region size for FPMA and FPMB. This confirms that our analysis is robust to the exact choice of background spectral extraction region, and that our background region accurately models the instrumental and astrophysical background underlying our source region.

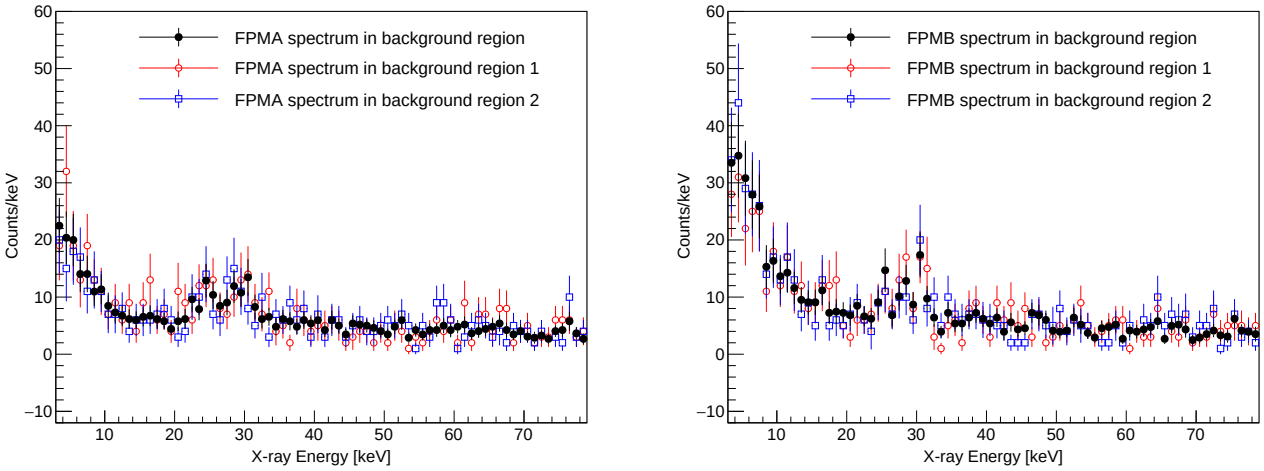

(a)FPMA (b)FPMB

FIG. S4. X-ray spectra in 3–79 keV energy range from FPMA and FPMB in different background regions after the normalization of region size: the black is the spectrum from the polygon region shown in Fig. S3; the red and blue are for the other region choices (see text for details). The data is binned with the width of 1 keV for presentation. The error bars are are calculated by Sumw2 with ROOT.

CHANDRA OBSERVATION OF BETELGEUSE

As a cross-check of our results, we use a 5 ks *Chandra* observation of Betelgeuse. *Chandra* has lower, and better understood, instrument background than *NuSTAR*, but its low-energy range (<10 keV) makes it less powerful for constraining the expected ALP-induced spectrum. We thus use the Chandra data to verify that our derived 95% C.L. on $g_{a\gamma}$ is consistent with this low-background, low-energy dataset. We analyzed an archival *Chandra* observation, ObsID 3365, which used the ACIS-I configuration in FAINT mode and was taken on 16 December 2001. We reprocessed the data using the standard `chandra_repro` tool from the CIAO v.4.12 software, with updated calibration files (CALDB v4.9.2.0, [S12]). The resultant cleaned data had a 4.899 ks exposure. Fig. S5 shows the observation image for $0.3-8$ keV soft X-ray events from *Chandra*. The short exposure time and low count rates made analyzing background-subtracted spectra difficult. Rather, we used the new CIAO `aprates` tool, which computes values and limits for various parameters such as point source count rate and photon flux (`https://cxc.harvard.edu/ciao/threads/aprates/index.html`).

Upper limits for the $0.3-2.5$ keV energy range emission from Betelgeuse for ObsID 3365 were first reported by Posson-Brown et al. (2007) (see Table 4 there). We used the same source ($r = 4''$) and background ($r_{min} = 10''$, $r_{max} = 10''$) regions centered on the star's equatorial position, and with `aprates` calculated a 3σ upper limit that matched the reported upper limit count rate. We then extended our analysis to the $0.3-8$ keV energy range. The resultant upper limits are 4.6 counts, or 9.42×10^{-4} counts s^{-1}. By counting the total events in the energy range $0.3-8$ keV, the constrains on $g_{a\gamma}$ is set as $2.2\times10^{-11}\ GeV^{-1}$ for the most optimistic stellar model and $B_T = 3\ \mu G$, and $6.5\times10^{-11}\ GeV^{-1}$ for the most conservative stellar model and $B_T = 0.4\ \mu G$ for $m_a < 3.5\times10^{-11}\ eV$. These values are well within our excluded regions, and thus we confirm that our results are consistent with this low-energy dataset.

CONSTRAINTS ON $g_{a\gamma}\times\sqrt{B_T}$

As shown in Eq. S2, the ALP-photon flux scales as $g_{a\gamma}^4\cdot B_{\rm T}^2$. To separately discuss the uncertainty from Betelgeuse stellar model (t_{cc}) and magnetic field (B_T), we also present our results as the constraints on the production of $g_{a\gamma}$ and $\sqrt{B_T}$ in Fig. S6. We set a constraint of $1.2\times10^{-11}GeV^{-1}\sqrt{\mu G}$ for $m_a < 3.5\times10^{-11}$ eV for $t_{cc} = 1.55\times10^5$ yr, and $0.9\times10^{-11}GeV^{-1}\sqrt{\mu G}$ for $m_a < 5.5\times10^{-11}$ eV for $t_{cc} = 3.6$ yr.

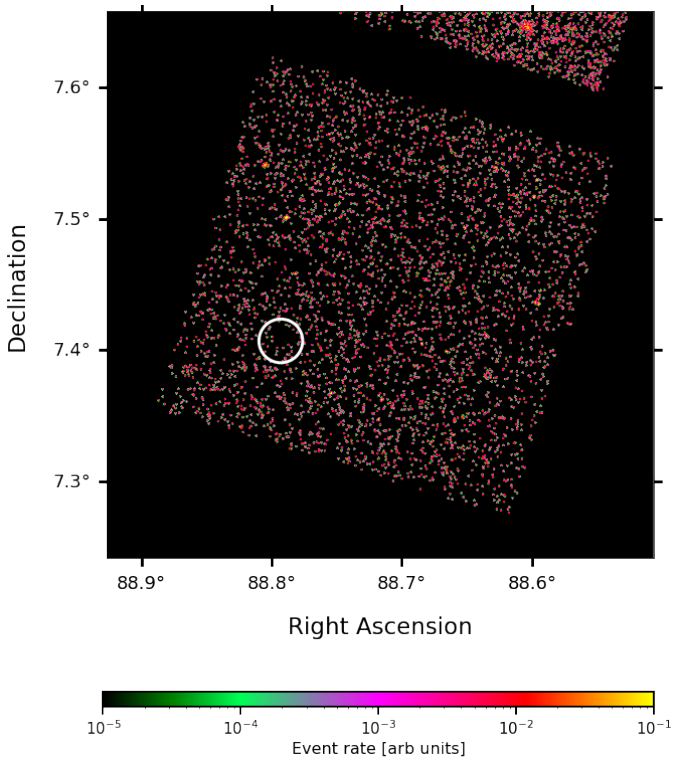

FIG. S5. Observation image for $0.3-8$ keV soft X-ray events from *Chandra*, the event rate is the relative value to the highest one and the image is smoothed with a 2-dimensional Gaussian of width $\sigma = 4.5''$ for presentation.The Betelgeuse source region is indicated with the white circle.

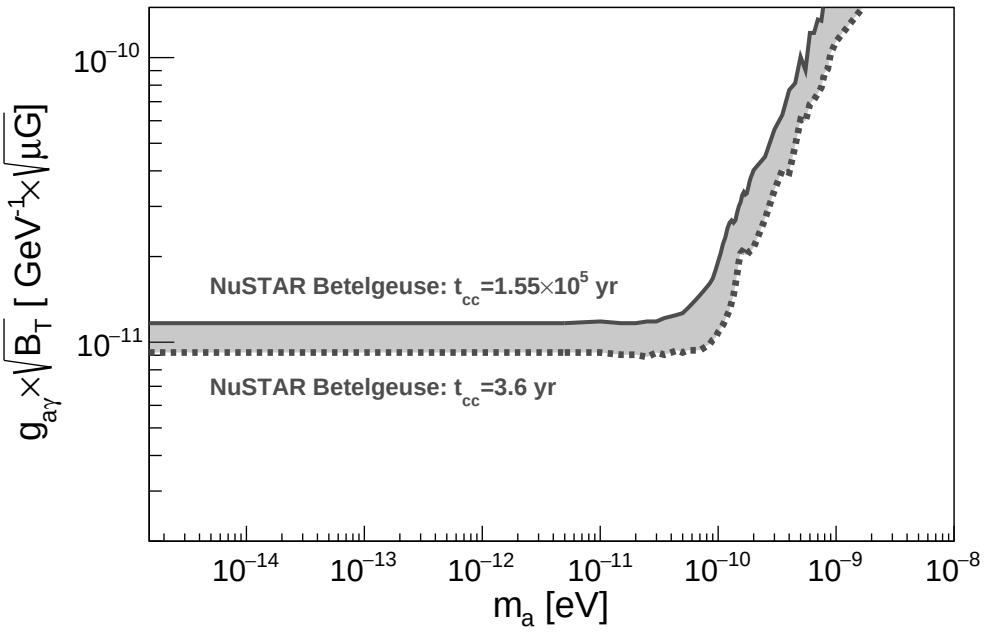

FIG. S6. Upper limits on $g_{a\gamma}\times\sqrt{B_T}$: the solid line is for the most conservative stellar model, dashed line for the most optimistic stellar model and the band for the other models between in.

EVOLUTION OF $g_{a\gamma}$ FOR MORE ALP MASSES

Fig. S7 illustrates the $g_{a\gamma}$ evolution as the remaining time for core collapse of Betelgeuse for more ALP masses.

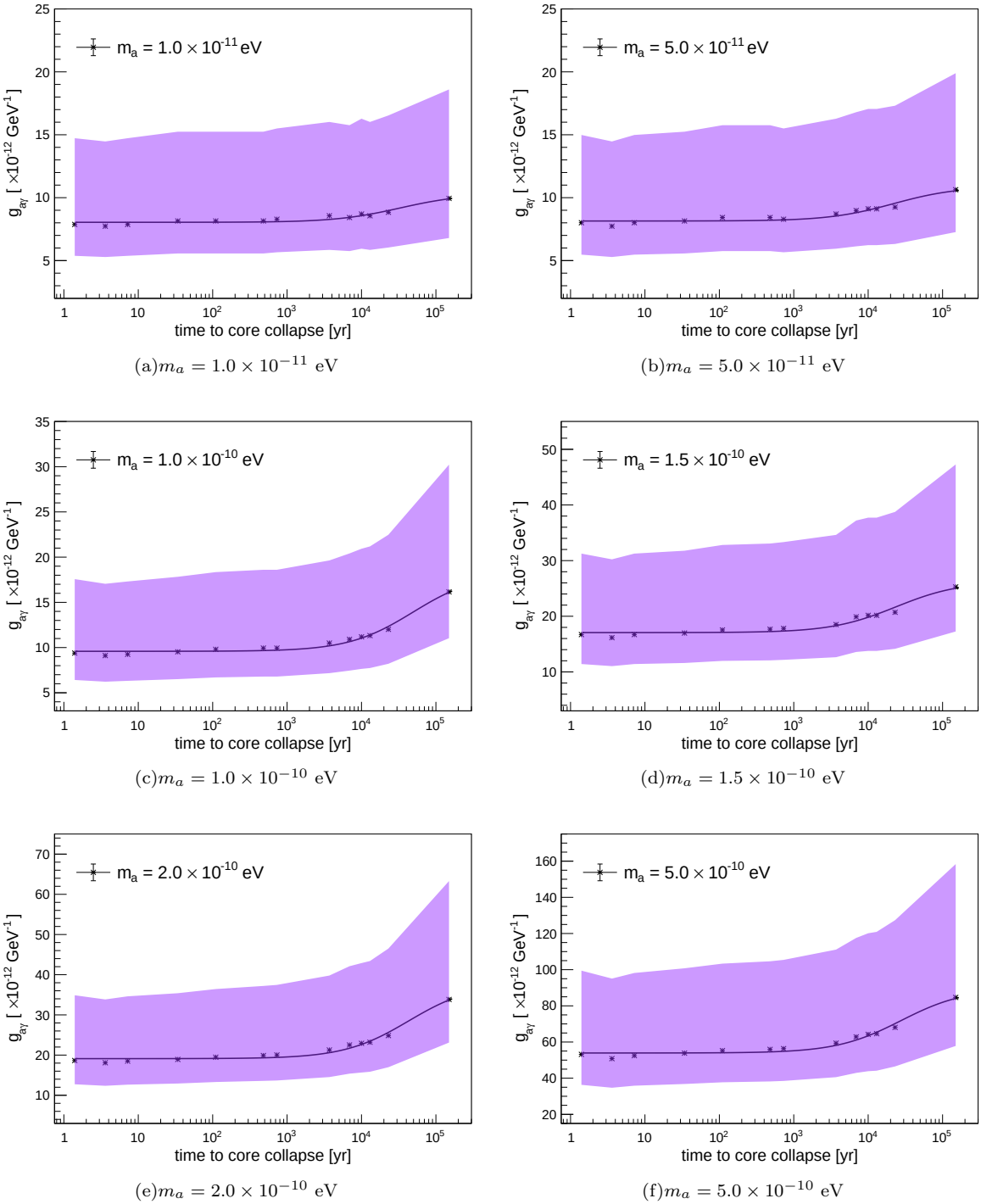

(a)$m_a = 1.0 \times 10^{-11}$ eV (b)$m_a = 5.0 \times 10^{-11}$ eV

(c)$m_a = 1.0 \times 10^{-10}$ eV (d)$m_a = 1.5 \times 10^{-10}$ eV

(e)$m_a = 2.0 \times 10^{-10}$ eV (f)$m_a = 5.0 \times 10^{-10}$ eV

FIG. S7. Evolution on the derived 95% C.L. upper limit of $g_{a\gamma}$ for different ALP masses with remaining time until core collapse for Betelgeuse. The points are the results with the assumption of $B_T = 1.4$ μG and the solid black line shows the fitting. The width of the violet band indicates the uncertainty due to choice of B_T.

[S1] S. Andriamonje *et al.* (CAST), "An Improved limit on the axion-photon coupling from the CAST experiment," JCAP **04**, 010 (2007), arXiv:hep-ex/0702006.

[S2] Oscar Straniero, Inma Dominguez, Luciano Piersanti, Maurizio Giannotti, and Alessandro Mirizzi, "The Initial Mass-Final Luminosity Relation of Type II Supernova Progenitors: Hints of New Physics?" Astrophys. J. **881**, 158 (2019), arXiv:1907.06367 [astro-ph.SR].

[S3] T. Le Bertre, L. D. Matthews, E. Gérard, and Y. Libert, "Discovery of a detached H I gas shell surrounding α Orionis," Mon. Not. R. Astron. Soc **422**, 3433–3443 (2012), arXiv:1203.0255 [astro-ph.SR].

[S4] G. Perrin, S. T. Ridgway, V. Coudé du Foresto, B. Mennesson, W. A. Traub, and M. G. Lacasse, "Interferometric observations of the supergiant stars α Orionis and α Herculis with FLUOR at IOTA," Astron. Astrophys **418**, 675–685 (2004), arXiv:astro-ph/0402099 [astro-ph].

[S5] D. L. Lambert, J. A. Brown, K. H. Hinkle, and Johnson, "Carbon, nitrogen and oxygem abundances in Betelgeuse," Astrophysical Journal **284**, 223–237 (1984).

[S6] G. Meynet, L. Haemmerlé, S. Ekström, C. Georgy, J. Groh, and A. Maeder, "The past and future evolution of a star like Betelgeuse," in *EAS Publications Series*, EAS Publications Series, Vol. 60, edited by P. Kervella, T. Le Bertre, and G. Perrin (2013) pp. 17–28, arXiv:1303.1339 [astro-ph.SR].

[S7] Michelle M. Dolan, Grant J. Mathews, Doan Duc Lam, Nguyen Quynh Lan, Gregory J. Herczeg, and David S. P. Dearborn, "Evolutionary Tracks for Betelgeuse," Astrophys. J. **819**, 7 (2016), arXiv:1406.3143 [astro-ph.SR].

[S8] D. R. Wik *et al.*, "NuSTAR Observations of the Bullet Cluster: Constraints on Inverse Compton Emission," Astrophys. J. **792**, 48 (2014), arXiv:1403.2722 [astro-ph.HE].

[S9] Kerstin Perez, Roman Krivonos, and Daniel R. Wik, "The Galactic Bulge Diffuse Emission in Broadband X-Rays with NuSTAR," Astrophys. J. **884**, 153 (2019), arXiv:1909.05916 [astro-ph.HE].

[S10] A. C. Fabian and X. Barcons, "The Origin of the X-Ray Background," Annu. Rev. Astron. Astrophys. **30**, 429–456 (1992).

[S11] Mikhail Revnivtsev, M. Gilfanov, R. Sunyaev, K. Jahoda, and C. Markwardt, "The Spectrum of the Cosmic X-Ray Background Observed by RTXE/PCA," Astron. Astrophys. **411**, 329–334 (2003), arXiv:astro-ph/0306569.

[S12] Antonella Fruscione, Jonathan C. McDowell, Glenn E. Allen, *et al.*, "CIAO: Chandra's data analysis system," Proc. SPIE, 6270, 62701V (2006), 10.1117/12.671760.